

Scalable Bayesian Inference for the Inverse Temperature of a Hidden Potts Model

Matthew T. Moores* Anthony N. Pettitt^{†‡}

Kerrie Mengersen^{†‡}

December 3, 2024

Abstract

The inverse temperature parameter of the Potts model governs the strength of spatial cohesion and therefore has a major influence over the resulting model fit. A difficulty arises from the dependence of an intractable normalising constant on the value of this parameter and thus there is no closed-form solution for sampling from the posterior distribution directly. There are a variety of computational approaches for sampling from the posterior without evaluating the normalising constant, including the exchange algorithm and approximate Bayesian computation (ABC). A serious drawback of these algorithms is that they do not scale well for models with a large state space, such as images with a million or more pixels. We introduce a parametric surrogate model, which approximates the score function using an integral curve. Our surrogate model incorporates known properties of the likelihood, such as heteroskedasticity and critical temperature. We demonstrate this method using synthetic data as well as remotely-sensed imagery from the Landsat-8 satellite. We achieve up to a hundredfold improvement in the elapsed runtime, compared to the exchange algorithm or ABC. An open source implementation of our algorithm is available in the R package **bayesImageS**.

1 Introduction

Markov random field (MRF) models have seen widespread use in image analysis since their introduction by Besag [1974], as surveyed by Winkler [2003] and Li [2009]. A MRF is a generalisation of the Markovian dependence structure to more than one dimension: satellite imagery has two spatial dimensions, while

*Department of Statistics, University of Warwick, Coventry CV4 7AL, UK

[†]Australian Research Council Centre for Excellence in Mathematical and Statistical Frontiers (ACEMS)

[‡]Mathematical Sciences School, Queensland University of Technology, Brisbane, Queensland 4001, Australia

Number of pixels	Satellite (900m ² /px)	CT slices (512×512)	HD Video 1080p
4 ⁶	3.7km ²
7 ⁶	105.9km ²	0.4	...
10 ⁶	900.0km ²	3.8	0.5
15 ⁶	10251.6km ²	43.5	5.5

Table 1: Scale of common types of images.

medical images such as computed tomography (CT) are three-dimensional. The hidden Potts [1952] model employs a latent MRF on discrete states to describe spatial dependence between adjacent neighbours. The degree of dependence in the model is governed by a parameter known as the inverse temperature due to its origin in statistical physics. It is difficult to set this parameter by trial and error, particularly for noisy images. Rather than using a fixed value, it would be preferable to estimate the inverse temperature as part of the model. However, the intractable normalising constant of the Potts model depends on the value of the inverse temperature. This means that there is no closed form solution for sampling from its posterior distribution, since the Metropolis-Hastings (M-H) ratio cannot be computed directly.

Rydén and Titterton [1998] derived a pseudolikelihood approximation [Besag, 1975] to the intractable posterior density. Gelman and Meng [1998] instead approximated the ratio of normalising constants using thermodynamic integration, also known as path sampling. Møller et al. [2006] introduced an auxiliary variable method that gives an exact Markov chain Monte Carlo (MCMC) algorithm for the special case of a 2 component Potts model, also known as an Ising model. Murray et al. [2006] proposed a variant of the exact method known as the exchange algorithm. By replacing the expensive perfect sampling step [Propp and Wilson, 1996] with an approximation such as Gibbs sampling, Cucala et al. [2009] developed an approximate exchange algorithm (AEA) that can be applied for Potts models with $k > 2$. Friel et al. [2009] introduced the reduced dependence approximation (RDA) which uses recursion to calculate the normalising constant on small sub-lattices. McGrory et al. [2012] generalised RDA to an irregular lattice. Grelaud et al. [2009] used the sufficient statistic of the Potts model to estimate the inverse temperature using approximate Bayesian computation (ABC). Everitt [2012] combined AEA with particle MCMC and also implemented ABC with sequential Monte Carlo (SMC-ABC) for the Ising model. Everitt found that the computational costs of both AEA and ABC were dominated by simulation of the auxiliary variable. While exact inference is theoretically possible, its applicability is limited to datasets with fewer than a thousand pixels. Comparisons such as McGrory et al. [2009], Moores and Mengersen [2014] and Moores et al. [2015] have shown that auxiliary variable methods are infeasible for the scale of data that is regularly encountered in image analysis.

Images containing multiple megapixels are now commonplace, from digital

photography and high-definition (HD) video to medical imaging and remote sensing. Table 1 illustrates how the number of pixels translates to real world scale for various types of images, including the area covered by a satellite image, the number of axial slices of a CT scan, and the number of frames of HD video. There is often the need to use multiple images to cover the spatial (and temporal) extent of an imaging study. Multispectral images from the Landsat-7 [NASA, 2011] and Landsat-8 [USGS, 2016] satellites have a spatial resolution of 30 metres per pixel (area of 900m^2). A Landsat image covers an area of approximately 170km north-south by 183km east-west. Tomographic reconstructions such as CT scans are usually represented as 3D image stacks, with 512×512 pixels per slice. The pixel resolution and slice width varies depending on the clinical protocol. A single frame of HD video is typically 1920×1080 pixels with 24 frames per second (fps), although higher frame rates and resolutions (such as ultra high definition, UHD) are available. The volumes of data involved in video processing necessitate specialised methods, which are beyond the scope of this paper. For examples of Bayesian methods for video analysis, see Simoncelli [1999], Minvielle et al. [2010], and the references therein. The remainder of the discussion will focus on static 2D images.

Scalable inference for intractable likelihoods is an active area of research. Some algorithms have been able to improve their runtime while still targeting the exact posterior distribution. For example, both Russian roulette [Lyne et al., 2015] and lazy ABC [Prangle, 2016] used random truncation of the likelihood computation. Liang et al. [2016] used an auxiliary chain to define an importance sampling (IS) distribution for the exchange algorithm. Sherlock et al. [2017] used k -nearest neighbours (k NN) combined with delayed acceptance [Christen and Fox, 2005] to accelerate pseudo-marginal MCMC. Compared to the exchange algorithm or ABC, these “exact-approximate” methods have provided an improvement in computational efficiency of an order of magnitude or less. This is not always sufficient to meet the practical requirements of real world applications.

For Bayesian inference to be feasible on large image datasets, it is necessary to sacrifice some degree of accuracy in order to achieve further improvements in speed. A variety of approximate methods have recently been proposed, which provide a tradeoff between accuracy and computational cost. One particular class of methods, known as Bayesian indirect likelihood [BIL; Drovandi et al., 2011, 2015], employs a surrogate model to approximate the likelihood function. BIL accelerates computation by interpolating between previous values of the auxiliary variables. It can also take advantage of massively parallel hardware to initialise the surrogate model using a precomputation step. Moores et al. [2015] used linear interpolation to accelerate ABC for the hidden Potts model. Conrad et al. [2016] used local polynomial or Gaussian process (GP) models to accelerate MCMC. Wilkinson [2014] and Meeds and Welling [2014] used GP emulation for ABC, while Drovandi et al. [2018] used a GP in a pseudo-marginal algorithm. Järvenpää et al. [2016] used a heteroskedastic GP model and demonstrated how the output of the precomputation step could be used for Bayesian model choice. The IS [Liang et al., 2016] and k NN [Sherlock et al., 2017] approaches could also

be viewed as forms of BIL. These nonparametric surrogate models approximate the likelihood under fairly generic assumptions regarding its functional form.

In this paper, we introduce the parametric functional approximate Bayesian (PFAB) algorithm for the Potts model. This algorithm incorporates a surrogate model that approximates the distribution of the sufficient statistic, therefore it is a type of BIL. The advantage over previous BIL algorithms is that we use a parametric integral curve that reflects the known properties of the intractable likelihood function, providing efficiency gains in comparison to nonparametric alternatives. We estimate the parameters of the function using a parallel pre-computation step. This leads to a great improvement in runtime, since there is no longer any need to simulate auxiliary variables during model fitting. Using a simulation study, we demonstrate empirically that this approximation error has very little impact on the resulting estimate of the posterior distribution. We also apply our algorithm to images from the Landsat-8 satellite, where the computational cost of AEA or ABC is very prohibitive. The superior scalability of PFAB makes it possible to perform fully Bayesian inference for demanding applications such as this.

The remainder of this article is organised as follows. The synthetic data and satellite imagery are described in Section 2. We define the hidden Potts model in Section 3 and examine the properties of its intractable normalising constant. Computational methods for estimating the inverse temperature, including the exchange algorithm, ABC and BIL, are reviewed in Section 4. We present our experimental results in Section 5 and conclude the article with a discussion.

2 Example datasets

2.1 Synthetic data

The inverse temperature cannot be directly observed, so the only way to measure the accuracy of a method is to use simulated data. We have adapted a method that was proposed by Cook et al. [2006] for the purpose of assessing the correctness of software for fitting a Bayesian model. Their central concept is to draw values of the model parameters from the prior and simulate data using those parameters, then fit the model and compare the estimate of the posterior distribution to the known value. We do not make use of the χ^2 test devised by Cook et al., since our goal is not to evaluate the hypothesis that our implementation of the algorithm is correct. We know that all three algorithms are approximations, therefore our aim is to compare the performance of these algorithms under various conditions.

We use a fixed number of 5 mixture components to generate 3 datasets containing 20 images each. The images within a dataset all have the same dimensions. The small images have $4^6 = 64 \times 64$ pixels; the medium images have $7^6 = 343 \times 343$; and the large images have $10^6 = 1000 \times 1000$. This enables us to study how the performance of the algorithms changes as the size of the images increases. We use a uniform prior to draw values of the inverse temperature.

This prior is adopted because it reflects current practice and enables comparison between our results and other recent studies. We use informative conjugate priors for the means and variances of the Gaussian mixture components. This corresponds with the model that we use in our applications to real data, as explained in Section 3.

2.2 Satellite remote sensing

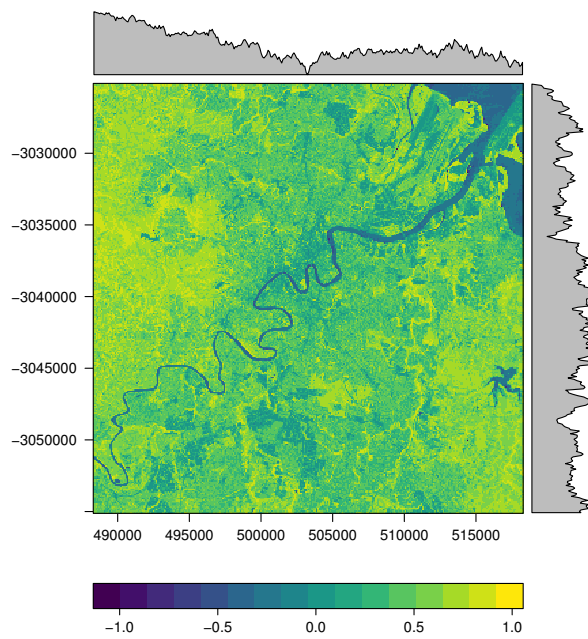
Abundant image data are available from Earth observation satellites. The size of satellite images and the frequency with which they are generated create a requirement for automated methods of image processing. Remotely sensed satellite imagery has been used for a variety of purposes, such as estimating land use [Small, 2001], water quality [McClain, 2009] and economic growth [Henderson et al., 2011]. In this study, we aim to classify the pixels in a satellite image according to the type and abundance of vegetation that is present. By labelling the pixels, we can quantify the levels of vegetation in an area and identify contiguous clusters of forest and parkland. These estimates could be used by environmental scientists to estimate global levels of plant biomass. Land use changes such as vegetation clearing could be detected by monitoring changes in pixel classification over time.

We apply our PFAB algorithm to analyse Landsat-8 imagery of Brisbane, Australia. The Landsat-8 satellite was launched in February 2013 and orbits the Earth every 16 days. To minimise artefacts, we only use imagery with less than 10% cloud cover. There are 18 such images available for 2015 and 2016. These images were cropped to a region of interest 30 km square, containing one million pixels. This roughly corresponds to the greater metropolitan area. An example of one of these images is shown in Fig. 1a. Images from Landsat-8 have 16 bits per pixel, with 55,000 possible values. This is an improvement over Landsat-5 and 7, which produce 8 bit images (256 values). The Landsat-8 bands are also narrower, which provides higher spectral resolution. The red visible light (VIS) band contains wavelengths between 636 and 673 nm, while the near-infrared (NIR) band is from 851 to 879 nm [USGS, 2016].

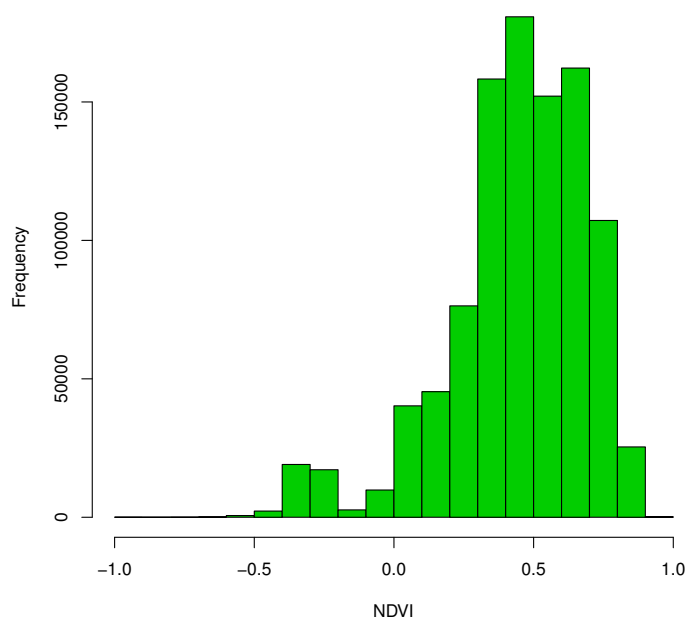
Metrics such as the normalised difference vegetation index (NDVI) use the ratio of reflectance of VIS and NIR light as a proxy for the abundance of chlorophyll [Tucker, 1979, Roy et al., 2016]:

$$\text{NDVI} = \frac{\text{NIR} - \text{VIS}}{\text{NIR} + \text{VIS}} \quad (1)$$

Land surface reflectance is estimated from Landsat-8 satellite imagery by correcting for atmospheric effects [Flood, 2014, Vermote et al., 2016]. When converted to NDVI, this produces numbers on a scale from -1 to +1. The distribution of NDVI values in the satellite image is illustrated by Fig. 1b. NDVI is generally used to detect vegetated areas, with an expected value for vegetation being between 0.3 and 0.8.



(a) Satellite image of Brisbane, Australia.



(b) Histogram of NDVI values.

Figure 1: A Landsat-8 satellite image and the distribution of pixel intensities.

3 Hidden Potts model

Image segmentation can be viewed as the task of labelling the observed pixels \mathbf{y} according to a finite set of discrete states $\mathbf{z} \in \{1, \dots, k\}$. The hidden Potts model allows for spatial correlation between neighbouring labels in the form of a Markov random field. The latent labels follow a Gibbs distribution, which is specified in terms of its conditional probabilities:

$$p(z_i | z_{\setminus i}, \beta) = \frac{\exp\{\beta \sum_{i \sim \ell} \delta(z_i, z_\ell)\}}{\sum_{j=1}^k \exp\{\beta \sum_{i \sim \ell} \delta(j, z_\ell)\}} \quad (2)$$

where β is the inverse temperature, $z_{\setminus i}$ represents all of the labels except z_i , $i \sim \ell$ are the neighbouring pixels of i , and $\delta(u, v)$ is the Kronecker delta function. Thus, $\sum_{i \sim \ell} \delta(z_i, z_\ell)$ is a count of the neighbours that share the same label.

If the labels z_i are indexed row-wise, the nearest (first-order) neighbours $i \sim \ell$ in a regular 2D lattice with c columns are $\{z_{i-1}, z_{i-c}, z_{i+c}, z_{i+1}\}$. Pixels situated at the boundary of the image domain have less than four neighbours. Likewise, voxels in a regular 3D lattice have a maximum of 6 first-order neighbours. These neighbourhood relationships are reciprocal, so $h \in i \sim \ell$ implies $i \in h \sim \ell$. If \mathcal{E} is the set of all unique neighbour pairs, or edges in the image lattice, then $|\mathcal{E}| = 2(n - \sqrt{n})$ for a square lattice and $3(n - n^{2/3})$ for a cube.

The observation equation links the latent labels to the corresponding pixel values:

$$p(\mathbf{y} | \mathbf{z}, \boldsymbol{\theta}) = \prod_{i=1}^n p(y_i | z_i, \theta_{z_i}) \quad (3)$$

where θ_j are the parameters that govern the distribution of the pixel values with label j . The hidden Potts model can thus be viewed as a spatially-correlated generalisation of the finite mixture model [Rydén and Titterton, 1998]. Green and Richardson [2002] used a Poisson likelihood for (3), with intensity λ_j . Instead we follow Geman and Geman [1984], Alston et al. [2007], and many others in assuming that the pixels with label j share a common mean μ_j corrupted by additive Gaussian noise with variance σ_j^2 :

$$y_i | z_i = j, \mu_j, \sigma_j^2 \sim \mathcal{N}(\mu_j, \sigma_j^2) \quad (4)$$

The Gibbs distribution is a member of the exponential family and so there is a sufficient statistic for this model, as noted by Grelaud et al. [2009]:

$$S(\mathbf{z}) = \sum_{i \sim \ell \in \mathcal{E}} \delta(z_i, z_\ell) \quad (5)$$

This statistic represents the total number of like neighbour pairs in the image. The augmented likelihood $p(\mathbf{y}, \mathbf{z} | \boldsymbol{\theta}, \beta)$ can therefore be factorised into $p(\mathbf{y} | \mathbf{z}, \boldsymbol{\theta}) p(S(\mathbf{z}) | \beta)$, where the second factor does not depend on the observed data, but only on the sufficient statistic. The joint posterior is then:

$$p(\boldsymbol{\theta}, \beta, \mathbf{z} | \mathbf{y}) \propto p(\mathbf{y} | \mathbf{z}, \boldsymbol{\theta}) \pi(\boldsymbol{\theta}) p(S(\mathbf{z}) | \beta) \pi(\beta) \quad (6)$$

The conditional distributions $p(\boldsymbol{\theta}|\mathbf{z}, \mathbf{y})$ and $p(z_i|z_{\setminus i}, \beta, y_i, \boldsymbol{\theta}_{z_i})$ can be simulated using Gibbs sampling, but $p(\beta|\mathbf{y}, \mathbf{z}, \boldsymbol{\theta})$ involves an intractable normalising constant $\mathcal{C}(\beta)$:

$$p(\beta | \mathbf{y}, \mathbf{z}, \boldsymbol{\theta}) = \frac{p(\mathbf{S}(\mathbf{z})|\beta)\pi(\beta)}{\int_{\beta} p(\mathbf{S}(\mathbf{z})|\beta)\pi(d\beta)} \quad (7)$$

$$\propto \frac{\exp\{\beta \mathbf{S}(\mathbf{z})\}}{\mathcal{C}(\beta)} \pi(\beta) \quad (8)$$

The normalising constant is also known as a partition function in statistical physics. It has computational complexity of $\mathcal{O}(nk^n)$, since it involves a sum over all possible combinations of the labels $\mathbf{z} \in \mathcal{Z}$:

$$\mathcal{C}(\beta) = \sum_{\mathbf{z} \in \mathcal{Z}} \exp\{\beta \mathbf{S}(\mathbf{z})\} \quad (9)$$

It is infeasible to calculate this value exactly for nontrivial images, thus computational approximations are required.

The conditional expectation of $\mathbf{S}(\mathbf{z})$ given β can be expressed in terms of the normalising constant:

$$\mathbb{E}_{\mathbf{z}|\beta}[\mathbf{S}(\mathbf{z})] = \frac{d}{d\beta} \log\{\mathcal{C}(\beta)\} \quad (10)$$

As β approaches infinity, all of the pixels in the image are almost surely assigned the same label, thus the expectation of $\mathbf{S}(\mathbf{z})$ approaches the total number of edges $|\mathcal{E}|$ asymptotically, while the variance approaches zero. When $\beta = 0$, (2) simplifies to $(\sum_j \exp\{0\})^{-1}$, hence the probability of any pair of neighbours being assigned the same label follows an independent Bernoulli distribution with $p = k^{-1}$. In this case, $\mathbf{S}(\mathbf{z})$ follows a Binomial distribution with expectation $|\mathcal{E}|/k$ and variance $|\mathcal{E}|k^{-1}(1 - k^{-1})$. In a finite image lattice the distribution of $\mathbf{S}(\mathbf{z})$ changes smoothly between these two extremes, as illustrated by Figure 2, but its computation is intractable for nontrivial images.

The score function of the Potts model is the difference between the observed sufficient statistic and its expectation:

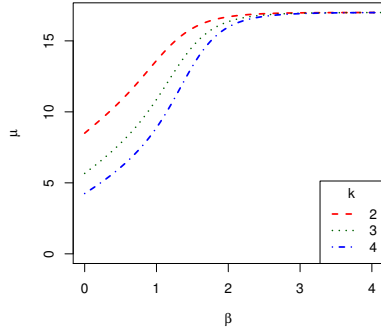
$$\frac{d}{d\beta} \log\{p(\mathbf{S}(\mathbf{z}) | \beta)\} = \mathbf{S}(\mathbf{z}) - \mathbb{E}_{\mathbf{z}|\beta}[\mathbf{S}(\mathbf{z})] \quad (11)$$

The variance of the score function, also known as the Fisher information, is given by the expectation of the derivative of (10):

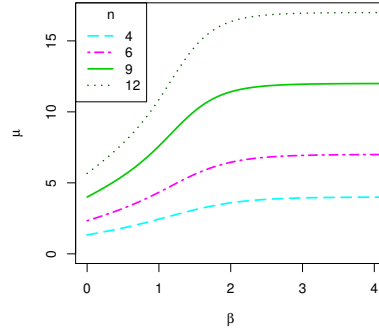
$$\mathcal{I}(\beta) = \mathbb{E}_{\mathbf{z}|\beta} \left[\left(\frac{d}{d\beta} \log\{p(\mathbf{S}(\mathbf{z}) | \beta)\} \right)^2 \right] \quad (12)$$

$$= \mathbb{E}_{\mathbf{z}|\beta} \left[\frac{d^2}{d\beta^2} \log\{\mathcal{C}(\beta)\} \right] \quad (13)$$

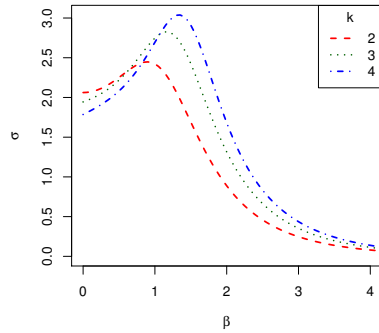
The Potts model undergoes a phase transition at the critical value of β , switching from a disordered to an ordered state. Potts [1952] showed that the



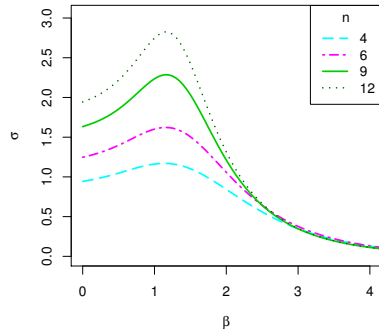
(a) Expectation for $n = 12$ and increasing values of $k \in \{2, 3, 4\}$.



(b) Expectation for $k = 3$ and increasing values of $n \in \{4, 6, 9, 12\}$.



(c) Standard deviation for $n = 12$ and increasing values of $k \in \{2, 3, 4\}$.



(d) Standard deviation for $k = 3$ and increasing values of $n \in \{4, 6, 9, 12\}$.

Figure 2: Distribution of the sufficient statistic of the Potts model for increasing values of the inverse temperature β , the number of pixels n , and the number of unique labels k . The expectation and standard deviation of $S(\mathbf{z})$ were calculated exactly, using a brute force method.

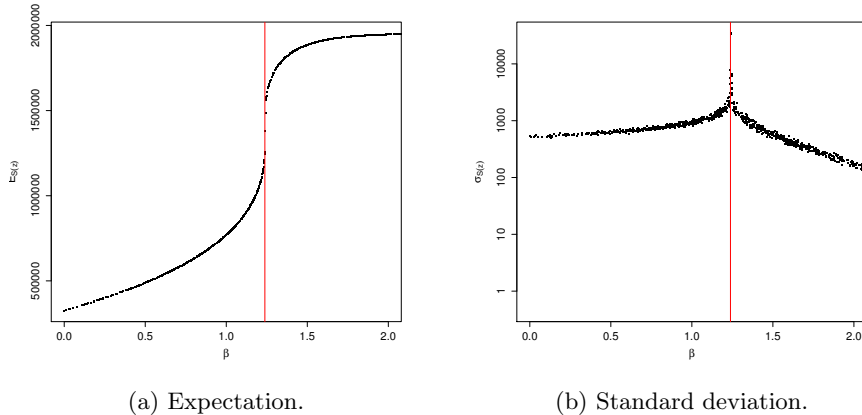


Figure 3: Approximate distribution of $S(\mathbf{z})$ using Swendsen-Wang for a 2D image with $k = 5$ and $|\mathcal{E}| = 1,998,000$. The vertical line is the critical value of β .

critical value for a 2D lattice on a cylinder can be calculated exactly according to:

$$\beta_{crit} = \log \left\{ 1 + \sqrt{k} \right\} \quad (14)$$

The periodic boundary condition does not apply to the lattices considered in this paper, so for example the critical value for the images in Figure 2 is different to (14). However, the error introduced by the finite boundary diminishes as n increases. Figure 3 shows that (14) is very accurate in predicting the behaviour of $S(\mathbf{z})$ for a 2D image with a maximum value of $S(\mathbf{z})$ for first-order neighbours of 1,998,000. This corresponds to the satellite image described in Section 2.2, with $k=5$ mixture components and $\beta_{crit} \approx 1.174$. $S(\mathbf{z})$ is approximated by simulation using the algorithm of Swendsen and Wang [1987]. Figure 3a shows that the gradient of the expectation becomes very steep near the critical region, which is reflected in the super-exponential increase of the standard deviation illustrated by Figure 3b. As $n \rightarrow \infty$ the derivative of the likelihood at the critical point, and hence the variance, is unbounded [Pickard, 1987]. This heteroskedasticity has important implications for the methods discussed in Section 4.

4 Computational methods

In this section we present three different approaches to simulating parameter values from (8) without computing the intractable normalising constant. We describe these algorithms in terms of Metropolis-within-Gibbs sampling to enable direct comparison, although we also mention other approaches where applicable, such as particle-based (SMC and PMCMC) methods. Reference implementations of all of these methods are available from various sources de-

scribed below, but for our purposes we have reimplemented the algorithms using `RcppArmadillo` [Eddelbuettel and Sanderson, 2014]. An R source package containing our code is available from CRAN [Moores and Mengersen, 2018].

4.1 Exchange algorithm

Algorithm 1 Exchange Algorithm

- 1: Initialise $\beta_0, \boldsymbol{\mu}_0, \boldsymbol{\sigma}_0^2, \mathbf{z}_0$
- 2: **for** $t = 1, \dots, T$ **do**
- 3: Update the labels $z_i \sim p(y_i | z_i, \mu_{z_i}, \sigma_{z_i}^2) p(z_i | z_{\setminus i}, \beta) \forall i \in \{1, \dots, n\}$
- 4: Calculate sufficient statistics $\mathbf{S}(\mathbf{z})$ and $\bar{y}_j, s_j^2 \forall z_i = j, \forall j \in \{1, \dots, k\}$
- 5: Update the noise parameters $\mu_j, \sigma_j^2 \sim p(\bar{y}_j, s_j^2 | \mu_j, \sigma_j^2) \pi(\mu_j | \sigma_j^2) \pi(\sigma_j^2)$
- 6: Draw proposed parameter value $\beta' \sim q(\beta' | \beta_{t-1})$
- 7: Generate $\mathbf{w} | \beta'$ by sampling from Equation (2)
- 8: Calculate the Radon-Nikodým derivative according to Equation (8):

$$\rho_t = \frac{\pi(\beta') q(\beta_{t-1} | \beta') \exp\{\beta' \mathbf{S}(\mathbf{z})\} \mathcal{C}(\beta_{t-1}) \exp\{\beta_{t-1} \mathbf{S}(\mathbf{w})\} \mathcal{C}(\beta')}{\pi(\beta_{t-1}) q(\beta' | \beta_{t-1}) \exp\{\beta_{t-1} \mathbf{S}(\mathbf{z})\} \mathcal{C}(\beta') \exp\{\beta' \mathbf{S}(\mathbf{w})\} \mathcal{C}(\beta_{t-1})} \quad (15)$$

- 9: Draw $u \sim \text{Uniform}[0, 1]$
 - 10: **if** $u < \min(1, \rho_t)$ **then**
 - 11: $\beta_t \leftarrow \beta'$
 - 12: **else**
 - 13: $\beta_t \leftarrow \beta_{t-1}$
 - 14: **end if**
 - 15: **end for**
-

Møller et al. [2006] demonstrated that it is possible to simulate from the posterior distribution of β by introducing an auxiliary variable, so that $\mathcal{C}(\beta)$ cancels out in the M-H ratio (15). The exchange algorithm of Murray et al. [2006] improves the performance of this method and avoids the need for a fixed estimate of β . The drawback of this approach is that it requires perfect sampling from the stationary distribution of the Potts model. This is possible for the special case of $k = 2$ using coupling from the past [Propp and Wilson, 1996, Huber, 2016] but even then it can be computationally prohibitive, particularly for large images. McGrory et al. [2009] reported that the time required for perfect sampling increased sharply for larger values of β . For this reason, Cucala et al. [2009] substitute 500 iterations of Gibbs sampling on the auxiliary variable to produce an approximate sample from its stationary distribution. This approximate exchange algorithm (AEA) can also be applied for Potts models with $k > 2$, where the state space \mathcal{Z} is only partially ordered. The details of this method are shown in Algorithm 1.

The ratio given by (15) can be considerably simplified if a uniform prior is used for $\pi(\beta)$ and β' is drawn from a symmetric proposal density. In this case, $\log\{\rho_t\}$ simplifies to $(\beta' - \beta_{t-1})\mathbf{S}(\mathbf{z}) + (\beta_{t-1} - \beta')\mathbf{S}(\mathbf{w})$. An implementation

of the exchange algorithm is available in the online supplementary material accompanying Friel and Pettitt [2011]. Everitt [2012] provides source code for AEA with particle MCMC.

In most cases, the number of iterations T required for the primary chain will depend on the mixing time of the checkerboard Gibbs sampler that is used in Step 4. This depends on both the size of the state vector \mathbf{z} and the value of β . The Gibbs sampler is not guaranteed to be ergodic for $\beta > \beta_{crit}$, so this is an important consideration when analysing real image data. In Sect. 5, we obtain a conservative estimate of the mixing time as part of the precomputation step and use this to guide our choice of T . Similarly, the heuristic number of 500 iterations advocated by Cucala et al. [2009], Everitt [2012] for simulating \mathbf{w} in AEA will be insufficient for large images when $\beta > \beta_{crit}$. Liang [2010] showed that convergence of the auxiliary chain could be improved by initialising \mathbf{w} at the current value of \mathbf{z} . Using this warm start, the number of required iterations depends on the autocorrelation time of the Markov chain, which can be an order of magnitude less than the mixing time. We use the Swendsen-Wang algorithm to simulate \mathbf{w} because this has better mixing properties for large values of β .

4.2 Approximate Bayesian computation

Like the exchange algorithm, ABC uses an auxiliary variable \mathbf{w} to decide whether to accept or reject the proposed value of β' . Instead of a M-H ratio such as (15), the summary statistics of the auxiliary variable and the observed data are directly compared. The proposal is accepted if the distance between these summary statistics is within the ABC tolerance, ϵ . This produces the following approximation when the labels \mathbf{z} are observed without error:

$$p(\beta | \mathbf{z}) \approx \pi_\epsilon(\beta | \|\mathbf{S}(\mathbf{w}) - \mathbf{S}(\mathbf{z})\| < \epsilon) \quad (16)$$

where $\|\cdot\|$ is a suitable norm. In this paper we simply use the absolute difference between $\mathbf{S}(\mathbf{w})$ and $\mathbf{S}(\mathbf{z})$, since the summary statistic (5) is univariate. $\mathbf{S}(\mathbf{z})$ is sufficient for β , as noted by Grelaud et al. [2009], therefore the ABC approximation (16) approaches the true posterior as $n \rightarrow \infty$ and $\epsilon \rightarrow 0$. In practice there is a tradeoff between the number of parameter values that are accepted and the size of the ABC tolerance.

Everitt [2012] introduced ABC for noisy data, such as the Ising model, but only when the observations are discrete and so $\mathbf{S}(\mathbf{y})$ is defined. Moores et al. [2015] showed that ABC can also be applied when the domain of the observed data is continuous, such as with the additive Gaussian noise of Equation (4). In this type of model the posterior distribution of β does not depend directly on the observed data \mathbf{y} , as shown by Equation (7). The ABC approximation (16) for the hidden Potts model becomes:

$$p(\beta | \mathbf{y}, \mathbf{z}, \boldsymbol{\theta}) \approx \pi_\epsilon(\beta | \|\mathbf{S}(\mathbf{w}) - \mathbf{S}(\mathbf{z})\| < \epsilon) \quad (17)$$

The other parameters can be updated using the current value of β and then the summary statistic $\mathbf{S}(\mathbf{z})$ can be computed from the current values of the labels,

using an ABC within Gibbs approach as shown in Algorithm 2. Equation (17) can be considered as a moving target, since $S(\mathbf{z})$ could change whenever the labels are updated. As a consequence, ABC with noisy data can be more prone to getting stuck in low probability regions of the parameter space.

Algorithm 2 ABC-MCMC with noisy data

```

1: Initialise  $\beta_0, \boldsymbol{\mu}_0, \boldsymbol{\sigma}_0^2, \mathbf{z}_0$ 
2: for  $t = 1, \dots, T$  do
3:   Update the labels  $z_i \sim p(y_i|z_i, \mu_{z_i}, \sigma_{z_i}^2) p(z_i|z_{\setminus i}, \beta) \forall i \in \{1, \dots, n\}$ 
4:   Calculate sufficient statistics  $S(\mathbf{z})$  and  $\bar{y}_j, s_j^2 \forall z_i = j, \forall j \in \{1, \dots, k\}$ 
5:   Update the noise parameters  $\mu_j, \sigma_j^2 \sim p(\bar{y}_j, s_j^2 | \mu_j, \sigma_j^2) \pi(\mu_j | \sigma_j^2) \pi(\sigma_j^2)$ 
6:   Draw proposed parameter value  $\beta' \sim q(\beta' | \beta_{t-1})$ 
7:   Generate  $\mathbf{w} | \beta'$  by sampling from Equation (2)
8:   Draw  $u \sim \text{Uniform}[0, 1]$ 
9:   if  $u < \frac{\pi(\beta')q(\beta_{t-1}|\beta')}{\pi(\beta_{t-1})q(\beta'|\beta_{t-1})}$  and  $\|S(\mathbf{w}) - S(\mathbf{z})\| < \epsilon$  then
10:      $\beta_t \leftarrow \beta'$ 
11:   else
12:      $\beta_t \leftarrow \beta_{t-1}$ 
13:   end if
14: end for

```

Grelaud et al. [2009] used a rejection sampler, where the proposals are drawn independently from the prior and thus $q(\beta' | \beta_{t-1}) = \pi(\beta)$. The advantages of this approach are that the convergence of the algorithm is uniformly ergodic and also that the pseudo-data \mathbf{w} can be reused for multiple images. However, under a sparse or uninformative prior, too many proposals are rejected for this approach to be viable. The probability of accepting any of the β' decays rapidly as the size of the image increases. Instead we have based Algorithm 2 on the ABC-MCMC algorithm of Marjoram et al. [2003]. This form of ABC algorithm is best suited for direct comparison with the other intractable likelihood methods in this article.

There have been many extensions to ABC, as reviewed by Marin et al. [2012]. Of particular interest are adaptive ABC algorithms that automatically adjust the tolerance ϵ and the proposal bandwidth σ_{MH}^2 . ABC with sequential Monte Carlo (SMC-ABC) algorithms use a sequence of target distributions $\pi_{\epsilon_t}(\beta | \|S(\mathbf{w}) - S(\mathbf{z})\| < \epsilon_t)$ such that $\epsilon_1 > \epsilon_2 > \dots > \epsilon_T$, where the number of SMC iterations T can be determined dynamically using a stopping rule. The SMC-ABC algorithm of Drovandi and Pettitt [2011] uses multiple MCMC steps for each SMC iteration, while the algorithm of Del Moral et al. [2012] uses multiple replicates of the summary statistics for each particle. Everitt [2012] has provided a MATLAB implementation of SMC-ABC with the online supplementary material accompanying his paper.

The computational efficiency of ABC is dominated by the cost of drawing updates to the auxiliary variable, as reported by Everitt [2012]. Thus, we would expect that the execution time for ABC would be similar to the approx-

imate exchange algorithm. Various approaches to improving this runtime have recently been proposed, such as the synthetic likelihood of Wood [2010], the Gaussian process emulation of Wilkinson [2014], the quasi-likelihood of Cabras et al. [2014], and the “lazy ABC” of Prangle [2016]. Of particular interest are methods involving surrogate models, as discussed in the following section.

4.3 Bayesian indirect likelihood

The distribution of the summary statistics $f(\mathbf{S}(\mathbf{w}) \mid \beta)$ is independent of the observed data \mathbf{y} and the labels \mathbf{z} . By simulating pseudo-data for values of β , we can create a binding function $\phi(\beta)$ for a surrogate model $f_A(\mathbf{S}(\mathbf{w}) \mid \phi(\beta))$. This binding function can be reused across multiple datasets, amortising its computational cost. By replacing $\mathbf{S}(\mathbf{w})$ with our surrogate model, we avoid the need to simulate pseudo-data or auxiliary variables during model fitting. In Moores et al. [2015], we showed that a precomputed binding function could lead to two orders of magnitude improvement in the elapsed runtime for fitting the hidden Potts model, while also improving the convergence properties of the original ABC-SMC algorithm. This is known as nonparametric Bayesian indirect likelihood with summary statistics, or nsBIL [Drovandi et al., 2015]. In this section, we introduce a parametric binding function that takes advantage of the properties of the Potts model that were described in Section 3. We utilise this function to perform Bayesian indirect inference, as shown in Algorithm 3.

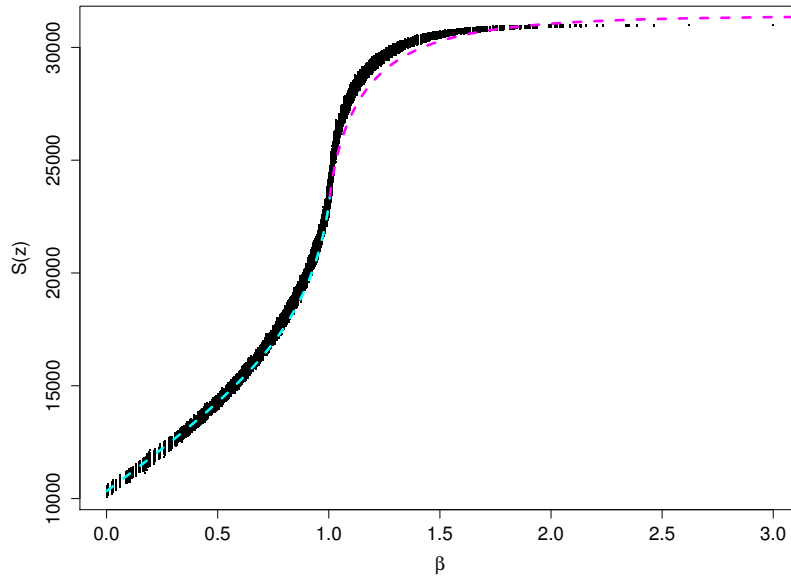
Algorithm 3 Parametric Functional Approximate Bayesian (PFAB) Algorithm

- 1: Generate $\mathbf{w}_s \mid \beta_s$ for sample points β_s , where $s = 1, \dots, S$
- 2: Fit the binding functions $\hat{\phi}_{\sigma^2}(\beta)$ & $\hat{\phi}_{\mu}(\beta)$
- 3: **for all** iterations $t = 1, \dots, T$ **do**
- 4: Update the labels $z_i \sim p(y_i \mid z_i, \mu_{z_i}, \sigma_{z_i}^2) p(z_i \mid z_{\setminus i}, \beta) \forall i \in \{1, \dots, n\}$
- 5: Calculate sufficient statistics $\mathbf{S}(\mathbf{z})$ and $\bar{y}_j, s_j^2 \forall z_i = j, \forall j \in \{1, \dots, k\}$
- 6: Update the noise parameters $\mu_j, \sigma_j^2 \sim p(\bar{y}_j, s_j^2 \mid \mu_j, \sigma_j^2) \pi(\mu_j \mid \sigma_j^2) \pi(\sigma_j^2)$
- 7: Draw proposed parameter value $\beta' \sim q(\beta' \mid \beta_{t-1})$
- 8: Approximate the Radon-Nikodým derivative:

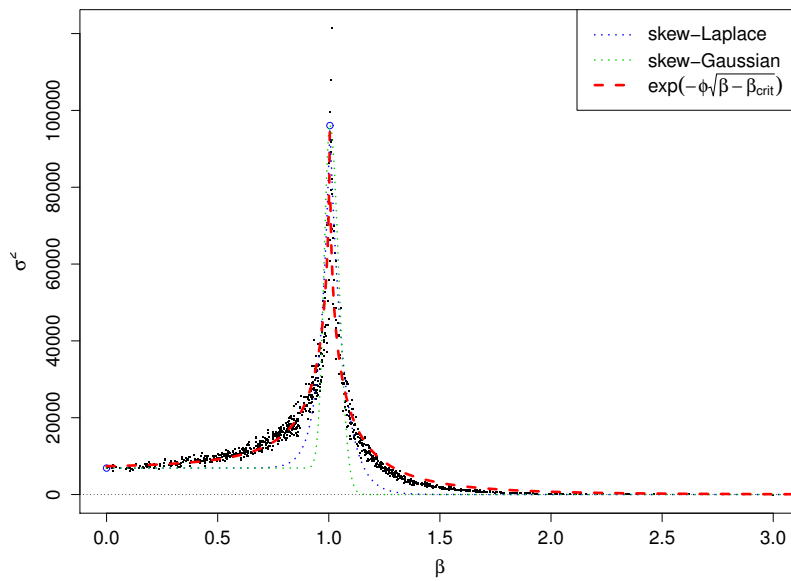
$$\rho = \frac{q(\beta_{t-1} \mid \beta') \pi(\beta') f_A(\mathbf{S}(\mathbf{z}) \mid \hat{\phi}_{\mu}(\beta'), \hat{\phi}_{\sigma^2}(\beta'))}{q(\beta' \mid \beta_{t-1}) \pi(\beta_{t-1}) f_A(\mathbf{S}(\mathbf{z}) \mid \hat{\phi}_{\mu}(\beta_{t-1}), \hat{\phi}_{\sigma^2}(\beta_{t-1}))}$$

- 9: Draw $u \sim \text{Uniform}[0, 1]$
 - 10: **if** $u < \min(1, \rho)$ **then**
 - 11: $\beta_t \leftarrow \beta'$ **else** $\beta_t \leftarrow \beta_{t-1}$
 - 12: **end if**
 - 13: **end for**
-

Figures 2 and 3 illustrate that $\mathbb{E}_{\mathbf{z} \mid \beta}[\mathbf{S}(\mathbf{z})]$ has the form of a sigmoid function, where the shape depends on the number of labels k and neighbours $|\mathcal{E}|$. The



(a) Parametric $\hat{\phi}_\mu(\beta)$



(b) Parametric $\hat{\phi}_{\sigma^2}(\beta)$

Figure 4: Binding functions for $S(\mathbf{w}) \mid \beta$ with $n = 5^6, k = 3$

variance of the distribution is equal to the gradient of this curve, according to (13). Clearly, piecewise-constant approximations such as k NN [Sherlock et al., 2017] or random forests [Pudlo et al., 2016] would be unsuitable as surrogate models. Even the piecewise linear model of Moores et al. [2015] can create issues for MCMC algorithms, due to sharp changes in the approximate variance. At the other end of the scale, GP approximations [Meeds and Welling, 2014] are too smooth to represent the phase transition boundary. Similarly, the generalised logistic function [Richards, 1959, Koya and Goshu, 2013] is not flexible enough to be used for this purpose.

Figure 4b illustrates three different approximations to the variance of the 2D Potts model with $k = 3$ and $n = 5^6$. The skew-Gaussian approximation is given by:

$$\hat{\phi}_{\sigma^2}(\beta) = \begin{cases} \mathbb{V}_0 + (\mathbb{V}_{max} - \mathbb{V}_0)e^{-\vartheta_1(\beta_{crit}-\beta)^2} & : 0 \leq \beta < \beta_{crit} \\ \mathbb{V}_{max}e^{-\vartheta_2(\beta_{crit}-\beta)^2} & : \beta \geq \beta_{crit} \end{cases} \quad (18)$$

The tails of the Gaussian decay much faster than the true model. The skew-Laplace approximation is slightly better:

$$\hat{\phi}_{\sigma^2}(\beta) = \begin{cases} \mathbb{V}_0 + (\mathbb{V}_{max} - \mathbb{V}_0)e^{-\vartheta_1(\beta_{crit}-\beta)} & : 0 \leq \beta < \beta_{crit} \\ \mathbb{V}_{max}e^{-\vartheta_2(\beta-\beta_{crit})} & : \beta \geq \beta_{crit} \end{cases} \quad (19)$$

The approximation can be further improved by taking the square root of the distance between β and its critical value:

$$\hat{\phi}_{\sigma^2}(\beta) = \begin{cases} \mathbb{V}_0 + (\mathbb{V}_{max} - \mathbb{V}_0)e^{-\vartheta_1\sqrt{\beta_{crit}-\beta}} & : 0 \leq \beta < \beta_{crit} \\ \mathbb{V}_{max}e^{-\vartheta_2\sqrt{\beta-\beta_{crit}}} & : \beta \geq \beta_{crit} \end{cases} \quad (20)$$

The binding function for the expectation is available in closed form (see Appendix A):

$$\hat{\phi}_{\mu}(\beta) = \begin{cases} \mathbb{E}_0 + \beta\mathbb{V}_0 + \int_0^\beta (\mathbb{V}_{max} - \mathbb{V}_0)e^{-\vartheta_1\sqrt{\beta_{crit}-\beta}} d\beta & : 0 \leq \beta < \beta_{crit} \\ \mathbb{E}_{\beta_{crit}} + \int_{\beta_{crit}}^\beta \mathbb{V}_{max}e^{-\vartheta_2\sqrt{\beta-\beta_{crit}}} d\beta & : \beta \geq \beta_{crit} \end{cases} \quad (21)$$

Figure 4a illustrates $\hat{\phi}_{\mu}(\beta)$ for the simulated dataset. The initial conditions \mathbb{E}_0 and \mathbb{V}_0 are known exactly, since the Potts model with $\beta = 0$ simplifies to a Binomial distribution. Pickard [1987] gives a formula for calculating \mathbb{V}_{max} , the variance at the critical point, in the asymptotic limit:

$$\lim_{|\mathcal{E}| \rightarrow \infty} \frac{S(\mathbf{w}) - \mathbb{E}_{\mathbf{z}|\beta_{crit}}[S(\mathbf{z})]}{\sqrt{|\mathcal{E}| \log\{|\mathcal{E}|\}}} \xrightarrow{d} \mathcal{N}\left(0, \frac{2}{\pi}\right) \quad (22)$$

We have found this formula useful as an upper bound, but in order to achieve a satisfactory fit with our surrogate model, we treat \mathbb{V}_1 and \mathbb{V}_2 as free parameters. This means that we estimate separate values of \mathbb{V}_{max} for $0 \leq \beta < \beta_{crit}$ and for $\beta \geq \beta_{crit}$.

n	$ \mathcal{E} $	ϑ_1	ϑ_2	$\sqrt{\mathbb{V}_1}$	$\sqrt{\mathbb{V}_2}$	$\mathbb{E}_{\beta_{crit}}/ \mathcal{E} $
64×64	8064	[4.569; 4.625]	[6.25; 6.27]	154	215	[0.7104; 0.7115]
343×343	234612	[4.690; 4.696]	[6.55; 6.59]	865	1089	[0.7626; 0.7633]
1000×1000	1998000	[4.715; 4.718]	[6.40; 6.42]	2547	3021	[0.7764; 0.7767]

Table 2: Posterior estimates for the parameters of the surrogate model.

There is a further issue with the Potts model for $k > 4$ labels, such as the $k = 5$ model studied in this paper. The model exhibits a first-order phase transition at the critical point [Baxter, 1973], which causes a discontinuity in the function $\hat{\phi}_\mu(\beta)$. To allow for this, we treat $\mathbb{E}_{\beta_{crit}}$ as a free parameter when $k > 4$. This leaves five parameters to estimate, $\Theta = \{\vartheta_1, \vartheta_2, \mathbb{V}_1, \mathbb{V}_2, \mathbb{E}_{\beta_{crit}}\}$, for any given values of $|\mathcal{E}|$ and $k > 4$.

At Step 1 of Algorithm 3 we select a set of sample points $\{\beta_s\}_{s=1}^S$. We know from the Fisher information (13) that we need more points close to β_{crit} , since that is where the variance is at its maximum. We selected $S = 72$ points for the experiments in Section 5, since we are able to generate pseudo-data independently, in parallel on a 36-core, hyper-threaded Intel Xeon server (a total of 72 virtual cores). This computation could easily be distributed across multiple servers if necessary, or run on a general-purpose graphical processing unit (GPU). However, we found that 72 points were sufficient to fit our parametric surrogate model. For each point, we ran 2,000 iterations of the Swendsen-Wang algorithm, discarding the first 500 as burn-in. When all of these parallel simulations are combined, we obtain a 72×1500 matrix of $S(\mathbf{w})$ values, conditional on β_s , $|\mathcal{E}|$, and k .

At Step 2, we use Stan [Carpenter et al., 2017] to sample from the posterior distribution $\pi(\Theta | S(\mathbf{w}), \beta_s)$, treating our matrix of simulations as observed data. Following the central limit theorem established by Pickard [1987], we approximate the distribution $f(S(\mathbf{w}) | \beta_s)$ using a truncated Gaussian:

$$f_A \left(S(\mathbf{w}) | \hat{\phi}_\mu(\beta_s), \hat{\phi}_{\sigma^2}(\beta_s) \right) \sim \mathcal{N} \left(\hat{\phi}_\mu(\beta_s), \hat{\phi}_{\sigma^2}(\beta_s) \right) \mathbb{1}_{(0 \leq S(\mathbf{w}) \leq |\mathcal{E}|)} \quad (23)$$

95% highest posterior density (HPD) intervals for Θ when $k = 5$ and using 3 different values of $|\mathcal{E}|$ for each of our simulated datasets are shown in Table 2. The values of ϑ_1 , ϑ_2 , and $\mathbb{E}_{\beta_{crit}}/|\mathcal{E}|$ are very similar for a range of image sizes. This indicates that informative priors could be used for these parameters, rather than the flat priors that we have used in our model. However, it is unclear how these parameters might change for different values of k .

5 Experimental results

5.1 Simulation study

We generated synthetic data using the R package `PottsUtils` [Feng, 2008, Feng and Tierney, 2011] as explained in Section 2.1. We used informative priors:

$$\pi(\boldsymbol{\mu}) \sim \mathcal{N}(\{-1.0, -0.5, 0.0, +0.5, +1.0\}, 0.1^2) \quad (24)$$

$$\pi(\sigma_j^2) \sim \mathcal{IG}(2.5, 0.06) \quad (25)$$

for the $j \in \{1, \dots, 5\}$ mixture components and a uniform prior on the interval $[0, 1.2\beta_{crit}]$ for the inverse temperature. β_{crit} was calculated using Equation (14) to be approximately equal to 1.174. We chose an upper bound of $1.2\beta_{crit} \approx 1.41$ because we found that simulated datasets with β above that value tended to have pixels with less than 5 unique labels. This was a particular problem with smaller images, where all of the pixels could be assigned the same label. The maximum value of β also affects the runtime, since the mixing of the Gibbs sampler slows dramatically for $\beta > \beta_{crit}$.

The precomputation step, running Swendsen-Wang for 2000 iterations with 72 different values of β , took 8.5 minutes for $n = 64^2$; 11.7 minutes for $n = 343^2$; and 38.9 minutes for $n = 1000^2$. We used 4 parallel chains with 10,000 iterations of the no u-turn sampler (NUTS) per chain to fit the parametric surrogate model in Stan. Half of the iterations were discarded as burn-in. This took 5.5 minutes on a 2.8GHz Intel Core *i7* laptop. The computational cost of fitting the surrogate model only depends on the number of iterations of Swendsen-Wang and NUTS, as well as the number of training points S , not on the sizes of the images involved. The parameters of the surrogate model are shown in Table 2.

The PFAB algorithm introduced in § 4.3, as well as accelerated ABC-MCMC using the nonparametric BIL approximation of Moores et al. [2015], were run for 20,000 iterations on each image, discarding the first 10,000 as burn-in. Due to the computational cost of the approximate exchange algorithm, it was run for only 5,000 iterations on the medium-sized images and 2,000 iterations on the images with 1 million pixels. The differences in elapsed runtime are illustrated by Figure 5d. The precomputation step for both PFAB and nsBIL-MCMC has reduced the elapsed runtime for images with $n = 343^2$ pixels from 5 hours for 5,000 iterations to only 15-23 minutes for 20,000 iterations. The runtime for $n = 1000^2$ pixels improved from 9-12 hours for 2,000 iterations of AEA to 2.5 hours for 20,000 iterations of PFAB or nsBIL.

The distributions of the differences between the MCMC samples of β and the true value of the inverse temperature are illustrated by Figure 5 for images with $n = 343^2$ pixels. Results for the other simulation studies are available in the supplementary material. The PFAB approximation to the posterior is overdispersed relative to AEA, but provides good coverage of the true β value. In contrast, nsBIL has the tendency to become stuck in a local mode for large values of β in the vicinity of the phase transition. This lack of ergodicity is a known problem with ABC-MCMC type algorithms [Lee and Łatuszyński, 2014],

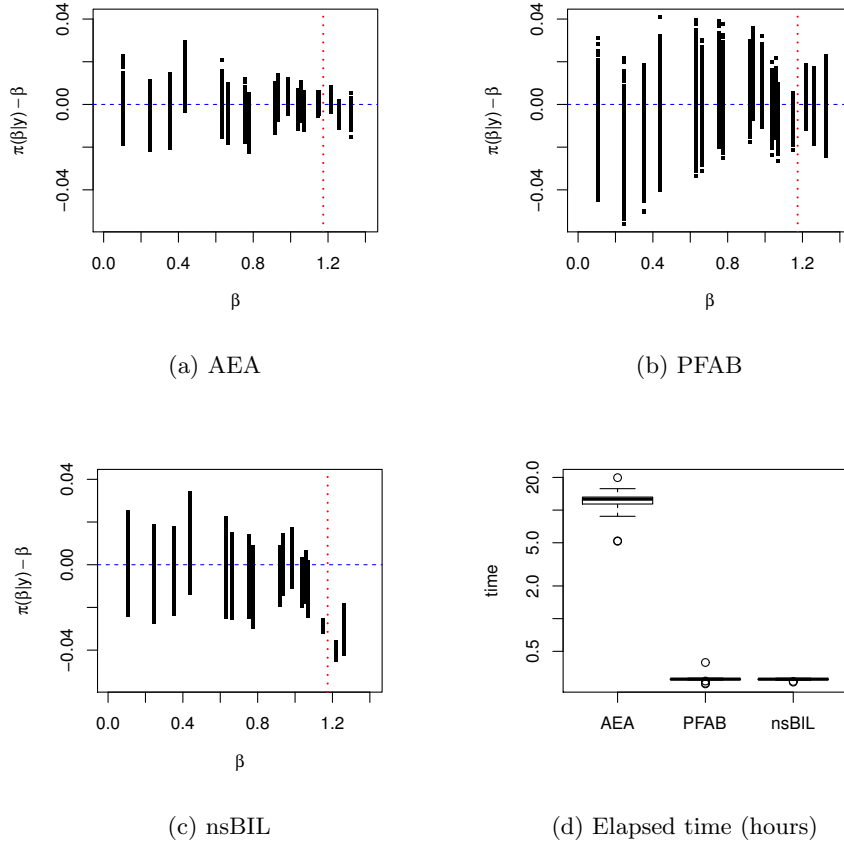


Figure 5: MCMC sampling for β in simulated data for 20 images with $k = 5$ and $n = 7^6$, using 3 different algorithms: (a) the approximate exchange algorithm (AEA); (b) our parametric functional approximate Bayesian (PFAB) algorithm; and (c) ABC-MCMC with a nonparametric surrogate model (nsBIL). The horizontal, dashed line indicates the true value of β , while the vertical, dotted line marks the critical point, β_{crit} . The elapsed runtimes of the 3 algorithms are shown in (d).

biasing the posterior towards underestimating β and hence under-smoothing the image pixels.

5.2 Satellite remote sensing

For the 18 satellite images described in Section 2.2 we used the same priors for μ_j (24), σ_j^2 (25), and β as for the simulation study. Since these images have the same dimensions (1000×1000 pixels) as the largest synthetic images, we could reuse the same surrogate models for PFAB and nsBIL. The reusability of surrogate models for many datasets is a major advantage of our approach.

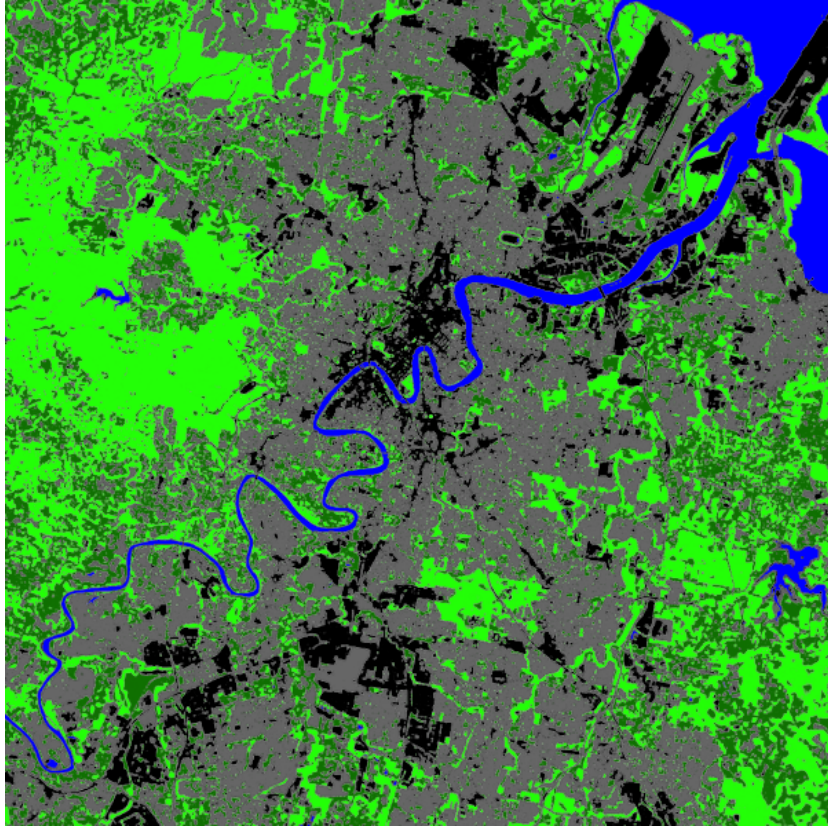
We were unable to evaluate accuracy for these images because the true values of the inverse temperature and the pixel labels are unknown. However, we can still compare the posterior distributions for β obtained from the three algorithms, as well as the time taken to fit the model. These results are summarised in Fig. 6. We ran PFAB and nsBIL for 20,000 iterations on each image, while the approximate exchange algorithm (AEA) was run for only 2,000 iterations, with 200 iterations of Swendsen-Wang for the auxiliary variables. AEA took 19 hours per image, while PFAB and nsBIL took 1.6 hours.

An example segmentation of one of the satellite images is shown in Fig. 6a. There is close correspondence between each of the 5 labels and categories of land use around Brisbane. The Brisbane River, Tingalpa Reservoir (in the south-east), and Enoggera Reservoir (in the north-west) are labelled in blue, while urbanised and industrial areas such as the central business district are labelled in black and the suburbs are labelled in grey. Large, forested areas, such as Mount Cotton and Mount Coot-tha, are labelled in green, as well as smaller features such as the City Botanic Gardens and New Farm Park. The histogram of pixel values with corresponding mixture model is shown in Fig. 6b.

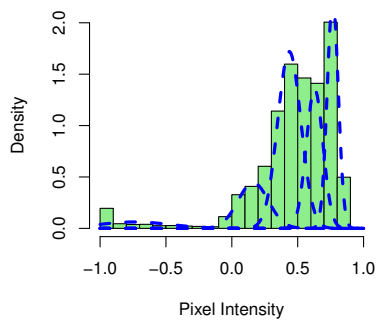
Fig 6c illustrates the posterior density plot for β obtained using the three algorithms. The posteriors from AEA and PFAB were generally in close agreement for the 18 images. As expected, the posterior from nsBIL is over-dispersed and uniformly-distributed over the interval $\pm \epsilon$. In one case, the nsBIL-MCMC algorithm failed to converge to the same value, most likely due to the issues with local modes that were observed in the simulation study.

6 Concluding remarks

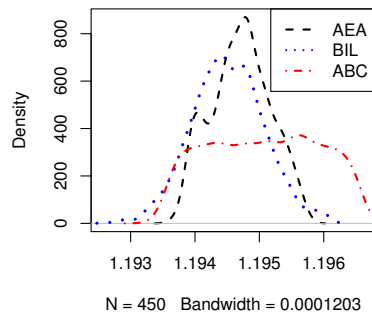
MCMC algorithms that involve simulating auxiliary variables at every iteration are too computationally expensive for applications in image analysis. Exact inference is infeasible for the scale of data that is commonly encountered in scientific studies, such as satellite remote sensing. Methods such as Russian roulette [Lyne et al., 2015], lazy ABC [Prangle, 2016], or delayed acceptance [Sherlock et al., 2017] can reduce the number of auxiliary iterations that need to be performed, but not enough to compensate for the two orders of magnitude difference in runtime that we observe.



(a) Image segmentation using 5 labels: water (blue); urban/industrial (black); suburbs (grey); parkland and forest (light/dark green)



(b) Mixture of Gaussians



(c) Posteriors for β

Figure 6: Results for the satellite image of Brisbane, Australia.

To address this problem, we have introduced a parametric functional approximate Bayesian (PFAB) algorithm. This algorithm incorporates known properties of the Potts model, such as the first-order phase transition for $k > 4$, to obtain a close approximation to the true density function. We fit our surrogate model using a precomputation step, which can be run independently in parallel for selected parameter values. The same surrogate model can be reused across multiple datasets, amortising its computational cost. The resulting posterior distribution for β has been shown to cover the true parameter value in simulation studies. When applied to real data, there is close agreement between the posterior densities obtained from PFAB and the exchange algorithm. Our approximation results in a hundred times speedup, making it feasible to use MCMC for images of realistic size, given reasonable computational power by contemporary standards. PFAB could also be used to accelerate other spatial Markov models, not only for image analysis.

The parameters of the surrogate model are similar for a range of different image sizes. This creates the possibility of fitting the model to smaller images and using the resulting posterior as an informative prior. Other methods for rescaling the Potts model, such as Cucala and Marin [2013], might also be applied in this context. It would also be interesting to explore how the parameters change for different values of k . Based on the trends evident in Fig. 2, it might be possible to interpolate between surrogate models for different n and k , without performing any additional simulations. PFAB might be used in combination with trans-dimensional algorithms or other methods of inference when k is unknown.

For the purpose of comparison, we have used random walk proposals for all three algorithms. However, the parametric surrogate model could be incorporated in an approximate Hamiltonian or Langevin algorithm [Strathmann et al., 2015, Zhang et al., 2017] to improve the efficiency of the MCMC sampler. Our surrogate model also provides an approximation to the Fisher information (13). This could be used in Bayesian optimisation to select design points for iterative refinement of the approximation, in a similar approach to Gutmann and Corander [2016] or Ryan et al. [2016].

A Parametric binding functions

The parametric binding function $\hat{\phi}_{\sigma^2}(\beta)$ was introduced in Section 4.3, where it was remarked that the corresponding expectation $\hat{\phi}_{\mu}(\beta) = \int_0^{\beta} \hat{\phi}_{\sigma^2}(\beta) d\beta$ was available in closed form. Since this function involves $|\beta_{crit} - \beta|$, the binding function $\hat{\phi}_{\mu}(\beta)$ is derived piecewise as $\int_0^{\beta_{crit}} \hat{\phi}_{\sigma^2}(\beta) d\beta + \int_{\beta_{crit}}^{\infty} \hat{\phi}_{\sigma^2}(\beta) d\beta$. This also allows for the second-order phase transition for $k > 4$ states, when there is a discontinuity at the critical point.

$$\hat{\phi}_{\mu}(\beta) = \begin{cases} \mathbb{E}_0 + \beta \mathbb{V}_0 + \int_0^{\beta} (\mathbb{V}_{max} - \mathbb{V}_0) \exp\{-\vartheta_1 \sqrt{\beta_{crit} - \beta}\} d\beta & : 0 \leq \beta < \beta_{crit} \\ \mathbb{E}_{\beta_{crit}} + \int_{\beta_{crit}}^{\beta} \mathbb{V}_{max} \exp\{-\vartheta_2 \sqrt{\beta - \beta_{crit}}\} d\beta & : \beta \geq \beta_{crit} \end{cases}$$

where $\mathbb{E}_{\beta_{crit}} = \int_0^{\beta_{crit}} \hat{\phi}_{\sigma^2}(\beta) d\beta$ if there is no discontinuity ($k \leq 4$) and is treated as a free parameter otherwise. The initial conditions \mathbb{E}_0 and \mathbb{V}_0 and the location of the phase transition β_{crit} are assumed known, whereas the remaining parameters $\{\vartheta_1, \vartheta_2, \mathbb{V}_{max}\}$ must be estimated from simulations.

For $0 \leq \beta < \beta_{crit}$:

$$\begin{aligned} \int_0^\beta \hat{\phi}_{\sigma^2}(\beta) d\beta &= \int_0^\beta \left(\mathbb{V}_0 + (\mathbb{V}_{max} - \mathbb{V}_0) \exp \left\{ -\vartheta_1 \sqrt{\beta_{crit} - \beta} \right\} \right) d\beta \\ &= \mathbb{E}_0 + \beta \mathbb{V}_0 + (\mathbb{V}_{max} - \mathbb{V}_0) \int_0^\beta \exp \left\{ -\vartheta_1 \sqrt{\beta_{crit} - \beta} \right\} d\beta \end{aligned}$$

By substitution:

$$\begin{aligned} &= \mathbb{E}_0 + \beta \mathbb{V}_0 - (\mathbb{V}_{max} - \mathbb{V}_0) \int_{\beta_{crit}}^{\beta_{crit} - \beta} \exp \left\{ -\vartheta_1 \sqrt{u} \right\} du \\ &= \mathbb{E}_0 + \beta \mathbb{V}_0 + 2(\mathbb{V}_{max} - \mathbb{V}_0) \int_{\sqrt{\beta_{crit} - \beta}}^{\sqrt{\beta_{crit}}} e^{-\vartheta_1 s} s ds \end{aligned}$$

By parts:

$$\begin{aligned} \int_{\sqrt{\beta_{crit} - \beta}}^{\sqrt{\beta_{crit}}} e^{-\vartheta_1 s} s ds &= \left[-\frac{s}{\vartheta_1 e^{\vartheta_1 s}} \right]_{\sqrt{\beta_{crit} - \beta}}^{\sqrt{\beta_{crit}}} + \frac{1}{\vartheta_1} \int_{\sqrt{\beta_{crit} - \beta}}^{\sqrt{\beta_{crit}}} e^{-\vartheta_1 s} ds \\ &= -\frac{1}{\vartheta_1} \left(\frac{\sqrt{\beta_{crit}}}{e^{\vartheta_1 \sqrt{\beta_{crit}}}} - \frac{\sqrt{\beta_{crit} - \beta}}{e^{\vartheta_1 \sqrt{\beta_{crit} - \beta}}} + \frac{1}{\vartheta_1 e^{\vartheta_1 \sqrt{\beta_{crit}}}} - \frac{1}{\vartheta_1 e^{\vartheta_1 \sqrt{\beta_{crit} - \beta}}} \right) \\ &= -\frac{1}{\vartheta_1^2} \left(\frac{\vartheta_1 \sqrt{\beta_{crit}} + 1}{e^{\vartheta_1 \sqrt{\beta_{crit}}}} - \frac{\vartheta_1 \sqrt{\beta_{crit} - \beta} + 1}{e^{\vartheta_1 \sqrt{\beta_{crit} - \beta}}} \right) \\ \int_0^\beta \hat{\phi}_{\sigma^2}(\beta) d\beta &= \mathbb{E}_0 + \beta \mathbb{V}_0 - 2 \frac{\mathbb{V}_{max} - \mathbb{V}_0}{\vartheta_1^2} \left(\frac{\vartheta_1 \sqrt{\beta_{crit}} + 1}{e^{\vartheta_1 \sqrt{\beta_{crit}}}} - \frac{\vartheta_1 \sqrt{\beta_{crit} - \beta} + 1}{e^{\vartheta_1 \sqrt{\beta_{crit} - \beta}}} \right) \end{aligned}$$

Similarly for $\beta \geq \beta_{crit}$:

$$\begin{aligned} \int_0^\beta \hat{\phi}_{\sigma^2}(\beta) d\beta &= \int_0^{\beta_{crit}} \hat{\phi}_{\sigma^2}(\beta) d\beta + \int_{\beta_{crit}}^\beta \hat{\phi}_{\sigma^2}(\beta) d\beta \\ &= \mathbb{E}_{\beta_{crit}} + \int_{\beta_{crit}}^\beta \left(\mathbb{V}_{max} e^{-\vartheta_2 \sqrt{\beta - \beta_{crit}}} \right) d\beta \end{aligned}$$

By substitution:

$$= \mathbb{E}_{\beta_{crit}} + 2\mathbb{V}_{max} \int_0^{\sqrt{\beta - \beta_{crit}}} e^{-\vartheta_2 s} s ds$$

By parts:

$$\begin{aligned} \int_0^{\sqrt{\beta - \beta_{crit}}} e^{-\vartheta_2 s} s ds &= -\frac{1}{\vartheta_2^2} \left(\frac{\vartheta_2 \sqrt{\beta - \beta_{crit}} + 1}{e^{\vartheta_2 \sqrt{\beta - \beta_{crit}}}} \right) \\ \int_0^\beta \hat{\phi}_{\sigma^2}(\beta) d\beta &= \mathbb{E}_{\beta_{crit}} - 2 \frac{\mathbb{V}_{max}}{\vartheta_2^2} \left(\frac{\vartheta_2 \sqrt{\beta - \beta_{crit}} + 1}{e^{\vartheta_2 \sqrt{\beta - \beta_{crit}}}} \right) \end{aligned}$$

Thus:

$$\hat{\phi}_\mu(\beta) = \begin{cases} \mathbb{E}_0 + \beta \mathbb{V}_0 - 2 \frac{\mathbb{V}_{max} - \mathbb{V}_0}{\vartheta_1^2} \left(\frac{1 + \vartheta_1 \sqrt{\beta_{crit}}}{\exp\{\vartheta_1 \sqrt{\beta_{crit}}\}} - \frac{1 + \vartheta_1 \sqrt{\beta_{crit} - \beta}}{\exp\{\vartheta_1 \sqrt{\beta_{crit} - \beta}\}} \right) & : 0 \leq \beta < \beta_{crit} \\ \mathbb{E}_{\beta_{crit}} - 2 \frac{\mathbb{V}_{max}}{\vartheta_2^2} \left(\frac{1 + \vartheta_2 \sqrt{\beta - \beta_{crit}}}{\exp\{\vartheta_2 \sqrt{\beta - \beta_{crit}}\}} \right) & : \beta \geq \beta_{crit} \end{cases}$$

References

- C. L. Alston, K. L. Mengersen, C. P. Robert, J. M. Thompson, P. J. Littlefield, D. Perry, and A. J. Ball. Bayesian mixture models in a longitudinal setting for analysing sheep CAT scan images. *Comput. Stat. Data Anal.*, 51:4282–4296, 2007. doi: 10.1016/j.csda.2006.05.013.
- R. J. Baxter. Potts model at the critical temperature. *J. Phys. C: Solid State Phys.*, 6(23):L445, 1973.
- J. Besag. Spatial interaction and the statistical analysis of lattice systems. *J. R. Stat. Soc. Ser. B*, 36(2):192–236, 1974.
- J. Besag. Statistical analysis of non-lattice data. *J. R. Stat. Soc. Ser. D*, 24(3):179–195, 1975.
- S. Cabras, M. Castellanos, and E. Ruli. A quasi likelihood approximation of posterior distributions for likelihood-intractable complex models. *METRON*, 72(2):153–167, 2014. doi: 10.1007/s40300-014-0040-5.
- B. Carpenter, A. Gelman, M. Hoffman, D. Lee, B. Goodrich, M. Betancourt, M. Brubaker, J. Guo, P. Li, and A. Riddell. Stan: A probabilistic programming language. *J. Statist. Soft.*, 76(1):1–32, 2017. doi: 10.18637/jss.v076.i01.
- J. A. Christen and C. Fox. Markov chain Monte Carlo using an approximation. *J. Comput. Graph. Stat.*, 14(4):795–810, 2005. doi: 10.1198/106186005X76983.
- P. R. Conrad, Y. M. Marzouk, N. S. Pillai, and A. Smith. Accelerating asymptotically exact MCMC for computationally intensive models via local approximations. *J. Am. Stat. Assoc.*, 111(516):1591–1607, 2016.
- S. R. Cook, A. Gelman, and D. B. Rubin. Validation of software for Bayesian models using posterior quantiles. *J. Comput. Graph. Stat.*, 15(3):675–692, 2006. doi: 10.1198/106186006X136976.
- L. Cucala and J.-M. Marin. Bayesian inference on a mixture model with spatial dependence. *J. Comput. Graph. Stat.*, 22(3):584–597, 2013. doi: 10.1080/10618600.2013.805652.
- L. Cucala, J.-M. Marin, C. P. Robert, and D. M. Titterton. A Bayesian reassessment of nearest-neighbor classification. *J. Am. Stat. Assoc.*, 104(485):263–273, 2009. doi: 10.1198/jasa.2009.0125.

- P. Del Moral, A. Doucet, and A. Jasra. An adaptive sequential Monte Carlo method for approximate Bayesian computation. *Stat. Comput.*, 22(5):1009–20, 2012. doi: 10.1007/s11222-011-9271-y.
- C. C. Drovandi and A. N. Pettitt. Estimation of parameters for macroparasite population evolution using approximate Bayesian computation. *Biometrics*, 67(1):225–233, 2011. doi: 10.1111/j.1541-0420.2010.01410.x.
- C. C. Drovandi, A. N. Pettitt, and M. J. Faddy. Approximate Bayesian computation using indirect inference. *J. R. Stat. Soc. Ser. C*, 60(3):317–337, 2011. doi: 10.1111/j.1467-9876.2010.00747.x.
- C. C. Drovandi, A. N. Pettitt, and A. Lee. Bayesian indirect inference using a parametric auxiliary model. *Stat. Sci.*, 30(1):72–95, 2015. doi: 10.1214/14-STS498.
- C. C. Drovandi, M. T. Moores, and R. J. Boys. Accelerating pseudo-marginal MCMC using Gaussian processes. *Comput. Stat. Data Anal.*, 118:1–17, 2018. doi: 10.1016/j.csda.2017.09.002.
- D. Eddelbuettel and C. Sanderson. RcppArmadillo: Accelerating R with high-performance C++ linear algebra. *Comput. Stat. Data Anal.*, 71:1054–63, 2014. doi: 10.1016/j.csda.2013.02.005.
- R. G. Everitt. Bayesian parameter estimation for latent Markov random fields and social networks. *J. Comput. Graph. Stat.*, 21(4):940–960, 2012. doi: 10.1080/10618600.2012.687493.
- D. Feng. *Bayesian hidden Markov normal mixture models with application to MRI tissue classification*. PhD thesis, University of Iowa, 2008.
- D. Feng and L. Tierney. *PottsUtils: Utility Functions of the Potts Models*, 2011. URL <http://CRAN.R-project.org/package=PottsUtils>. R package version 0.2-2.
- N. Flood. Continuity of reflectance data between Landsat-7 ETM+ and Landsat-8 OLI, for both top-of-atmosphere and surface reflectance: A study in the Australian landscape. *Remote Sens.*, 6(9):7952–7970, 2014. doi: 10.3390/rs6097952.
- N. Friel and A. N. Pettitt. Classification using distance nearest neighbours. *Stat. Comput.*, 21(3):431–437, 2011. doi: 10.1007/s11222-010-9179-y.
- N. Friel, A. N. Pettitt, R. Reeves, and E. Wit. Bayesian inference in hidden Markov random fields for binary data defined on large lattices. *J. Comp. Graph. Stat.*, 18(2):243–261, 2009. doi: 10.1198/jcgs.2009.06148.
- A. Gelman and X.-L. Meng. Simulating normalizing constants: from importance sampling to bridge sampling to path sampling. *Statist. Sci.*, 13(2):163–185, 1998. doi: 10.1214/ss/1028905934.

- S. Geman and D. Geman. Stochastic relaxation, Gibbs distributions and the Bayesian restoration of images. *IEEE Trans. PAMI*, 6:721–41, 1984.
- P. J. Green and S. Richardson. Hidden Markov models and disease mapping. *J. Am. Stat. Assoc.*, 97:1055–1070, 2002.
- A. Grelaud, C. P. Robert, J.-M. Marin, F. Rodolphe, and J.-F. Taly. ABC likelihood-free methods for model choice in Gibbs random fields. *Bayesian Analysis*, 4(2):317–336, 2009. doi: 10.1214/09-BA412.
- M. U. Gutmann and J. Corander. Bayesian optimization for likelihood-free inference of simulator-based statistical models. *J. Mach. Learn. Res.*, 17(1):4256–4302, 2016.
- V. Henderson, A. Storeygard, and D. N. Weil. A bright idea for measuring economic growth. *Am. Econ. Rev.*, 101(3):194–199, 2011. doi: 10.1257/aer.101.3.194.
- M. L. Huber. *Perfect Simulation*, volume 148 of *Monographs on Statistics & Applied Probability*. Chapman & Hall/CRC Press, Boca Raton, FL, 2016.
- M. Järvenpää, M. Gutmann, A. Vehtari, and P. Marttinen. Gaussian process modeling in approximate Bayesian computation to estimate horizontal gene transfer in bacteria. *arXiv:1610.06462 [stat.ML]*, 2016. URL <https://arxiv.org/abs/1610.06462>. arXiv preprint.
- P. R. Koya and A. T. Goshu. Solutions of rate-state equation describing biological growths. *Amer. J. Math. Stat.*, 3(6):305–311, 2013. doi: 10.5923/j.ajms.20130306.02.
- A. Lee and K. Latuszyński. Variance bounding and geometric ergodicity of Markov chain Monte Carlo kernels for approximate Bayesian computation. *Biometrika*, 101(3):655–671, 2014. doi: 10.1093/biomet/asu027.
- S. Z. Li. *Markov Random Field Modeling in Image Analysis*. Springer, Dordrecht, 3rd edition, 2009.
- F. Liang. A double Metropolis Hastings sampler for spatial models with intractable normalizing constants. *J. Stat. Comput. Sim.*, 80(9):1007–1022, 2010. doi: 10.1080/00949650902882162.
- F. Liang, I. H. Jin, Q. Song, and J. S. Liu. An adaptive exchange algorithm for sampling from distributions with intractable normalizing constants. *J. Am. Stat. Assoc.*, 111(513):377–393, 2016. doi: 10.1080/01621459.2015.1009072.
- A.-M. Lyne, M. Girolami, Y. Atchadé, H. Strathmann, and D. Simpson. On Russian roulette estimates for Bayesian inference with doubly-intractable likelihoods. *Statist. Sci.*, 30(4):443–467, 2015. doi: 10.1214/15-STS523.

- J.-M. Marin, P. Pudlo, C. P. Robert, and R. J. Ryder. Approximate Bayesian computational methods. *Stat. Comput.*, 22(6):1167–1180, 2012. doi: 10.1007/s11222-011-9288-2.
- P. Marjoram, J. Molitor, V. Plagnol, and S. Tavaré. Markov chain Monte Carlo without likelihoods. *Proc. Natl Acad. Sci.*, 100(26):15324–15328, 2003. doi: 10.1073/pnas.0306899100.
- C. R. McClain. A decade of satellite ocean color observations. *Ann. Rev. Mar. Sci.*, 1:19–42, 2009. doi: 10.1146/annurev.marine.010908.163650.
- C. A. McGrory, D. Titterton, R. Reeves, and A. N. Pettitt. Variational Bayes for estimating the parameters of a hidden Potts model. *Stat. Comput.*, 19(3): 329–340, 2009. doi: 10.1007/s11222-008-9095-6.
- C. A. McGrory, A. N. Pettitt, R. Reeves, M. Griffin, and M. Dwyer. Variational Bayes and the reduced dependence approximation for the autologistic model on an irregular grid with applications. *J. Comput. Graph. Stat.*, 21(3):781–796, 2012. doi: 10.1080/10618600.2012.632232.
- E. Meeds and M. Welling. GPS-ABC: Gaussian process surrogate approximate Bayesian computation. In *Proc. 30th Conf. UAI*, pages 593–602, Quebec City, Canada, 2014. AUAI Press.
- P. Minvielle, A. Doucet, A. Marrs, and S. Maskell. A Bayesian approach to joint tracking and identification of geometric shapes in video sequences. *Image and Vision Computing*, 28(1):111–123, 2010. doi: 10.1016/j.imavis.2009.05.002.
- J. Møller, A. N. Pettitt, R. Reeves, and K. K. Berthelsen. An efficient Markov chain Monte Carlo method for distributions with intractable normalising constants. *Biometrika*, 93(2):451–458, 2006. doi: 10.1093/biomet/93.2.451.
- M. T. Moores and K. Mengersen. Bayesian approaches to spatial inference: modelling and computational challenges and solutions. In *Proc. 33rd Int. Wkshp MaxEnt*, volume 1636 of *AIP Conf. Proc.*, pages 112–117, Canberra, Australia, 2014. Amer. Inst. Physics. doi: 10.1063/1.4903701.
- M. T. Moores and K. Mengersen. bayesImageS: Bayesian methods for image segmentation using a Potts model, 2018. URL <https://CRAN.R-project.org/package=bayesImageS>. R package version 0.5-0.
- M. T. Moores, C. C. Drovandi, K. Mengersen, and C. P. Robert. Pre-processing for approximate Bayesian computation in image analysis. *Stat. Comput.*, 25(1):23–33, 2015. doi: 10.1007/s11222-014-9525-6.
- I. Murray, Z. Ghahramani, and D. J. C. MacKay. MCMC for doubly-intractable distributions. In *Proc. 22nd Conf. UAI*, pages 359–366, Arlington, VA, 2006. AUAI Press.

- NASA. Landsat 7 science data users handbook. Technical report, National Aeronautics and Space Administration, Greenbelt, MD, 2011. URL <http://landsathandbook.gsfc.nasa.gov/>.
- D. K. Pickard. Inference for discrete Markov fields: The simplest nontrivial case. *J. Am. Stat. Assoc.*, 82(397):90–96, 1987. doi: 10.1080/01621459.1987.10478394.
- R. B. Potts. Some generalized order-disorder transformations. *Proc. Camb. Philos. Soc.*, 48:106–9, 1952. doi: 10.1017/S0305004100027419.
- D. Prangle. Lazy ABC. *Stat. Comput.*, 26(1):171–185, 2016. doi: 10.1007/s11222-014-9544-3.
- J. G. Propp and D. B. Wilson. Exact sampling with coupled Markov chains and applications to statistical mechanics. *Random Struct. Algor.*, 9(1–2):223–252, 1996. doi: 10.1002/(SICI)1098-2418(199608/09)9:1/2<223::AID-RSA14>3.0.CO;2-O.
- P. Pudlo, J.-M. Marin, A. Estoup, J.-M. Cornuet, M. Gautier, and C. P. Robert. Reliable ABC model choice via random forests. *Bioinformatics*, 32(6):859–866, 2016. doi: 10.1093/bioinformatics/btv684.
- F. J. Richards. A flexible growth function for empirical use. *J. Exp. Bot.*, 10(2):290–301, 1959. doi: 10.1093/jxb/10.2.290.
- D. P. Roy, V. Kovalsky, H. K. Zhang, E. F. Vermote, L. Yan, S. S. Kumar, and A. Egorov. Characterization of Landsat 7 to Landsat 8 reflective wavelength and normalized difference vegetation index continuity. *Remote Sens. Environ.*, 185:57–70, 2016. doi: 10.1016/j.rse.2015.12.024.
- C. M. Ryan, C. C. Drovandi, and A. N. Pettitt. Optimal Bayesian experimental design for models with intractable likelihoods using indirect inference applied to biological process models. *Bayesian Anal.*, 11(3):857–883, 2016. doi: 10.1214/15-BA977.
- T. Rydén and D. M. Titterton. Computational Bayesian analysis of hidden Markov models. *J. Comput. Graph. Stat.*, 7(2):194–211, 1998. doi: 10.1080/10618600.1998.10474770.
- C. Sherlock, A. Golightly, and D. A. Henderson. Adaptive, delayed-acceptance MCMC for targets with expensive likelihoods. *J. Comput. Graph. Stat.*, 26(2):434–444, 2017.
- E. P. Simoncelli. Bayesian multi-scale differential optical flow. In B. Jähne, H. Haussecker, and P. Geissler, editors, *Handbook of computer vision and applications*, volume 2, chapter 14, pages 397–422. Academic Press, San Diego, 1999.

- C. Small. Estimation of urban vegetation abundance by spectral mixture analysis. *Int. J. Remote Sens.*, 22(7):1305–1334, 2001. doi: 10.1080/01431160151144369.
- H. Strathmann, D. Sejdinovic, S. Livingstone, Z. Szabo, and A. Gretton. Gradient-free Hamiltonian Monte Carlo with efficient kernel exponential families. In *Adv. Neur. Inf. Proc. Sys. (NIPS)*, volume 28, pages 955–963. 2015.
- R. H. Swendsen and J.-S. Wang. Nonuniversal critical dynamics in Monte Carlo simulations. *Phys. Rev. Lett.*, 58:86–88, 1987. doi: 10.1103/PhysRevLett.58.86.
- C. J. Tucker. Red and photographic infrared linear combinations for monitoring vegetation. *Remote Sens. Environ.*, 8(2):127–150, 1979. doi: 10.1016/0034-4257(79)90013-0.
- USGS. Landsat 8 data users handbook. Technical Report LSDS-1574, United States Geological Survey, Sioux Falls, SD, March 2016. URL <https://landsat.usgs.gov/landsat-8-18-data-users-handbook>. version 2.0.
- E. Vermote, C. Justice, M. Claverie, and B. Franch. Preliminary analysis of the performance of the Landsat 8/OLI land surface reflectance product. *Remote Sens. Environ.*, 185:46–56, 2016. doi: 10.1016/j.rse.2016.04.008.
- R. D. Wilkinson. Accelerating ABC methods using Gaussian processes. In *Proc. 17th Int. Conf. AISTATS*, volume 33 of *JMLR W&CP*, pages 1015–1023, Reykjavik, Iceland, 2014. MIT Press.
- G. Winkler. *Image Analysis, Random Fields and Markov chain Monte Carlo Methods: A Mathematical Introduction*. Springer-Verlag, Berlin Heidelberg, 2nd edition, 2003.
- S. N. Wood. Statistical inference for noisy nonlinear ecological dynamic systems. *Nature*, 466(7310):1102–4, 2010. doi: 10.1038/nature09319.
- C. Zhang, B. Shahbaba, and H. Zhao. Precomputing strategy for Hamiltonian Monte Carlo method based on regularity in parameter space. *Comput. Stat.*, 32(1):253–279, 2017. doi: 10.1007/s00180-016-0683-1.

Acknowledgements

MTM was supported by the UK EPSRC as part of the “*i*-Like” programme grant (ref: EP/K014463/1). KLM was supported by an ARC Laureate Fellowship. KLM and ANP received funding from the ARC Centre of Excellence in Mathematical and Statistical Frontiers (ACEMS). The authors thank Geoff Nicholls, Christian Robert, Jean-Michel Marin, Daniel Simpson, and Clair Alston-Knox for helpful conversations during the preparation of this manuscript. Landsat imagery courtesy of NASA Goddard Space Flight Center and U.S. Geological Survey.